32nd Congress
of the International Council
of the Aeronautical Sciences
September 6-10, 2021
Pudong Shangri-La, Shanghai, China

AERODYNAMIC DESIGN THEORY AND METHODOLOGY FOR AN AIRFRAME-INLET INTEGRATED FULL-WAVERIDER VEHICLE

Feng Ding[1,2], Jun Liu[1,2], Wei Huang[1,2], Shanguang Guo[3*]

[1]College of Aerospace Science and Engineering, National University of Defense Technology, Changsha, Hunan 410073, People's Republic of China
[2]Science and Technology on Scramjet Laboratory, National University of Defense Technology, Changsha, Hunan 410073, People's Republic of China
[3]Corresponding author, Science and Technology on Plasma Dynamics Laboratory, Air Force Engineering University, Xi'an, Shanxi 710038, People's Republic of China

Abstract

With the aim of integrating a scramjet with an airframe, this study develops a novel aerodynamic design methodology for airframe/inlet integration for an air-breathing hypersonic waverider vehicle; this new type of vehicle is termed the 'full-waverider vehicle' in this study. This newly proposed design methodology not only enables waverider design of the forebody, fuselage belly, and wings of the vehicle but also effectively integrates the airframe and streamline tracing inlet while keeping the waverider characteristics of the entire vehicle intact. In this paper, first, the design principle and procedure of the full-waverider vehicle derived from an axisymmetric basic shock wave are described in detail. Second, the design methodologies of the full-waverider vehicle are validated by a numerical computation method. Third, the effects of the design parameters on the aerodynamic shapes and performances are also numerically analysed under both the on-design and off-design conditions. The obtained results show that the proposed aerodynamic design theory and methodology are effective for the design of the airframe/inlet integration of an air-breathing hypersonic waverider vehicle. At the same time, parameter sensitivity analysis shows that the waverider afterbody is a major factor in lift-to-drag ratio of the full-waverider vehicle, and the lift-to-drag ratio of the full-waverider vehicle is higher than that of the conventional waverider vehicle, owing to the high lift-to-drag ratio characteristics of the waverider afterbody.

Keywords: Air-breathing hypersonic waverider vehicle; aerodynamic design theory and methodology; airframe/inlet integrated full-waverider; aerodynamic characteristics; parameter sensitivity analysis.

1. Introduction

A large number studies conducted since the 1960s have shown that one of the key factors for ensuring the success of an air-breathing hypersonic vehicle is an effective design for the airframe/inlet integration [1]–[3].

The waverider first proposed by Nonweiler [4] in 1959 is any hypersonic lifting body with an

attached shock wave along its leading edge [5]–[12]. Since then, because of the excellent aerodynamic configuration of the waverider, it has become one of the most ideal aerodynamic configurations for hypersonic vehicles. As a result, over the past 60 years, design methodologies for airframe/inlet integrated waverider vehicles have been extensively studied by researchers.

Two classes of general methods exist for using the waverider concept in the design of air-breathing hypersonic vehicles [12]–[17], namely the waverider forebody/inlet integration design method, and the waverider airframe/inlet integration design method. Inspired by many predecessor's research on waverider airframe/inlet integration, Ding et al. [3] were the first to propose a novel airframe/inlet integration derived from an axisymmetric generating body. In their work, a basic flow model considering both internal and external flows was derived from an axisymmetric generating body by use of both the streamline tracing and the method of characteristics (MOC). Subsequently, the airframe/inlet integrated waverider vehicle was developed from the basic flow model by the streamline tracing method. With the aims of overcoming the limitations of the existing basic flow model derived from an axisymmetric generating body and extending the aerodynamic design method of the airframe/inlet integrated waverider vehicle, Ding et al. [5][6] developed an upgraded basic flow model derived from an axisymmetric shock wave. It then upgraded the design method for airframe/inlet integration of an air-breathing hypersonic waverider vehicle, which was termed the 'full-waverider vehicle' in their studies.

In this paper, in order to further develop the aerodynamic design theory and study the aerodynamic characteristics of the upgraded full-waverider vehicle, the upgraded design principle and method for the airframe/inlet integrated waverider vehicle based on an axisymmetric shock wave are described first. Second, several cases designed by the updated airframe/inlet integration design methodology are solved. Third, numerical computation methods employed to validate the upgraded design theory and methodology, and analyse the performances and viscous effect of the vehicle are presented; additionally, the effects of the design parameters on the aerodynamic shapes and performances are also presented.

2.   Design theory and method of a full-waverider vehicle

The vehicle developed according to the proposed design concept is termed the 'airframe/inlet integrated full-waverider vehicle' in this study, or the 'full-waverider vehicle' for short.

Figure 1 illustrates the basic design principle of the airframe/inlet integrated full-waverider methodology. Both the waverider forebody/inlet and the waverider afterbody of the full-waverider vehicle are derived from the same basic flow model. Figure 1(a) illustrates the upgraded basic flow model derived from an axisymmetric shock wave; four walls and three curved shock waves constitute this model.

As shown in Figure 1(b), under supersonic inflow conditions, an axisymmetric basic shock wave is taken as the initial condition, and then, both the waverider forebody and the waverider afterbody of the full-waverider vehicle are generated in the 3D flow field after the axisymmetric basic shock wave. The waverider afterbody is composed of the waverider fuselage belly and two waverider wings. As

shown in Figure 1(c), the forebody/inlet is generated by tracing the streamlines in the forebody/inlet basic flow region (i.e. region *A-B-C-G-F-E-D* as shown in Figure 1(a)), from the leading-edge curve of forebody (curve 2-4-7) and the inlet lip curve (curve 2-1-7) downstream, up to the inlet exit plane; this simultaneously yields the inlet exit curve (curve 10-12-11-13). Then, the waverider surfaces of the fuselage belly and two wings are generated by tracing the streamlines in the afterbody basic flow region (i.e. region *D-M-N-R* as shown in Figure 1(a)), from the inlet lip curve (curve 2-1-7) and the leading-edge curves of two wings (curves 3-2 and 7-17) downstream, up to the base plane; this also simultaneously yields the trailing-edge curve of the fuselage belly (curve 14-15-16) and the trailing-edge curves of two wings (curves 3-14 and 16-17).
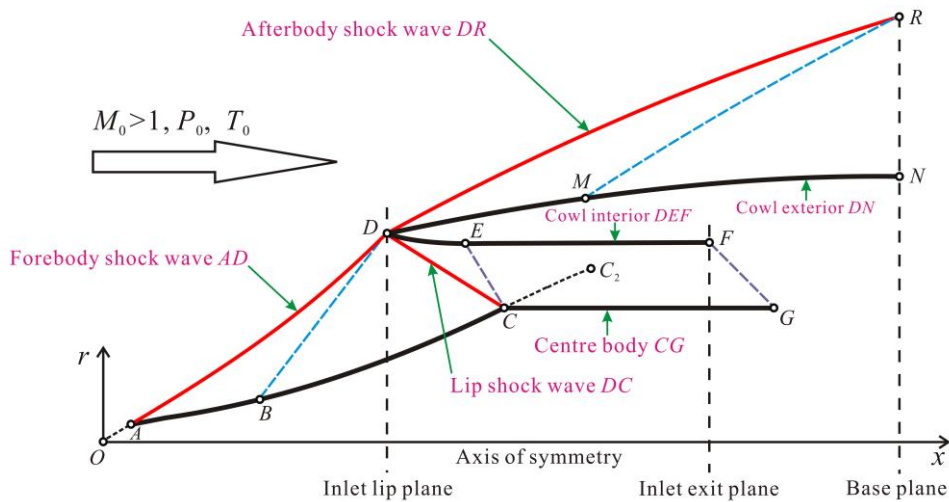
(a) Axisymmetric basic flow model derived from the axisymmetric shock wave
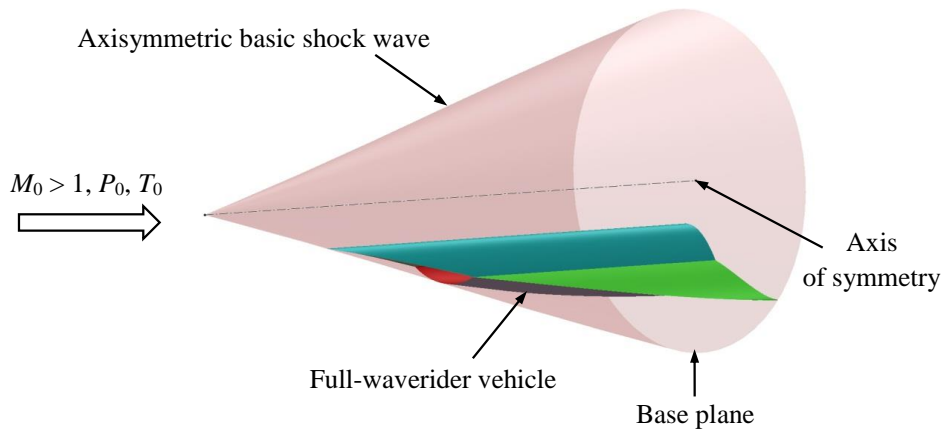
(b) Isentropic view of the full-waverider vehicle and shock wave
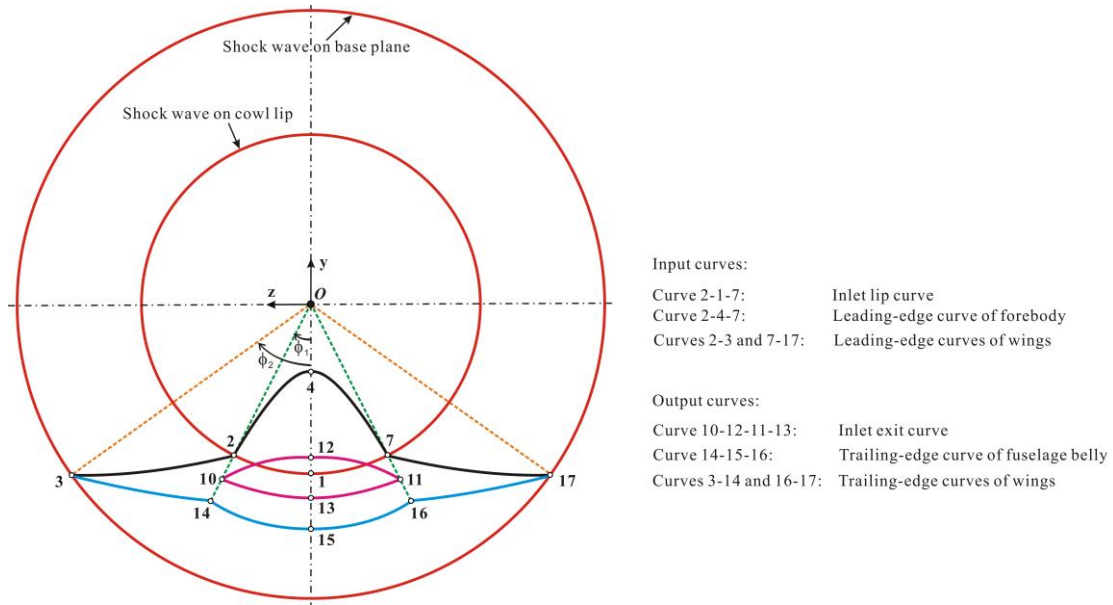
(c) Rear view of the geometric and shock wave curves

Figure 1 Schematic representation of the full-waverider vehicle and corresponding axisymmetric basic shock wave.

3. Physical model and numerical method

3.1 Physical model

In order to validate the design method and study the influence of design parameters of the basic flow model on the shape and performance of the full-waverider waverider, seven practical cases employing the upgraded full-waverider concept but with different design parameters are solved; another case employing a conventional waverider forebody/inlet integration method is also solved and used as a contrast case for comparative analysis. As in our past work [3][5][6], these cases have not considered the combustion chamber, nozzle, and control surfaces.
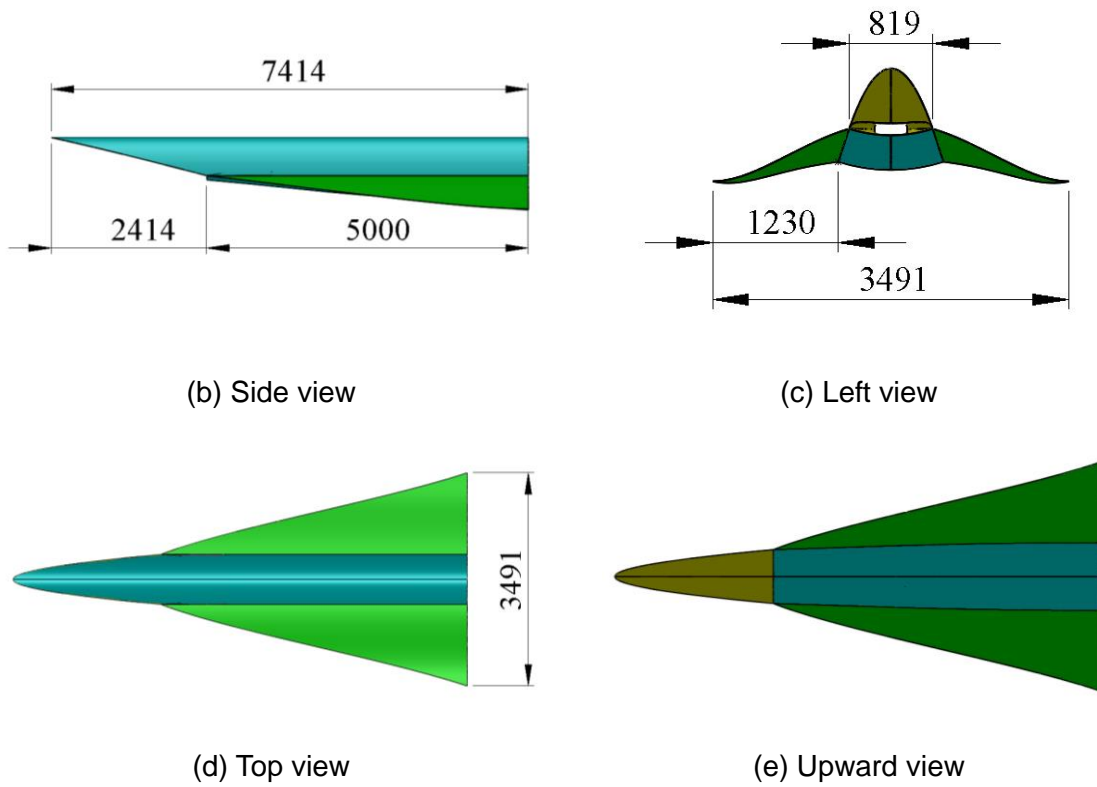

(a) 3D view

(b) Side view

(c) Left view

(d) Top view
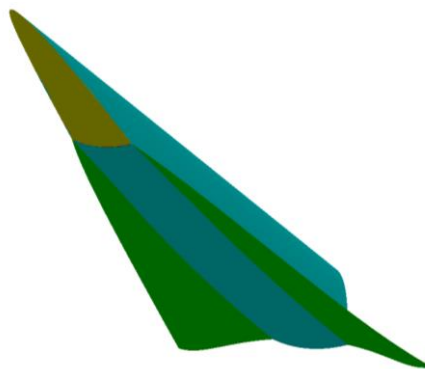
(e) Upward view
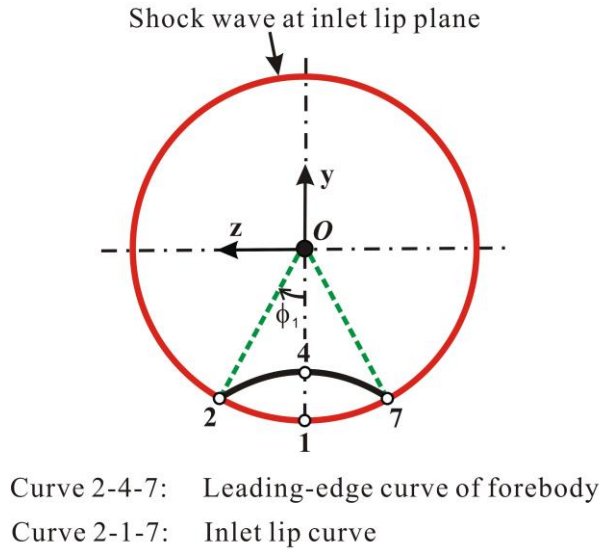
Figure 2 Geometric model for case3_FW.

3.1.1 Case3_FW derived from the full-waverider vehicle design method

Figure 2 shows the geometric model and size for the considered case generated by the full-waverider vehicle design method. It can be seen from Figure 2 that the length and width of the geometric model are about 7.4 m and 3.5 m, respectively, and the length of the forebody is about 2.4 m.

In this case, which is termed as case3_FW, the inlet design parameters at the inlet exit plane of the basic flow model are an average Mach number and average pressure rise ratio at the inlet exit of about 3.8 and 10.0, respectively. The specific design parameters and equations for the basic flow model and the input curves used for the design of the full-waverider vehicle can refer to our previous work [5][6].

(a) Forebody/inlet integrated axisymmetric basic flow model.

Shock wave at inlet lip plane
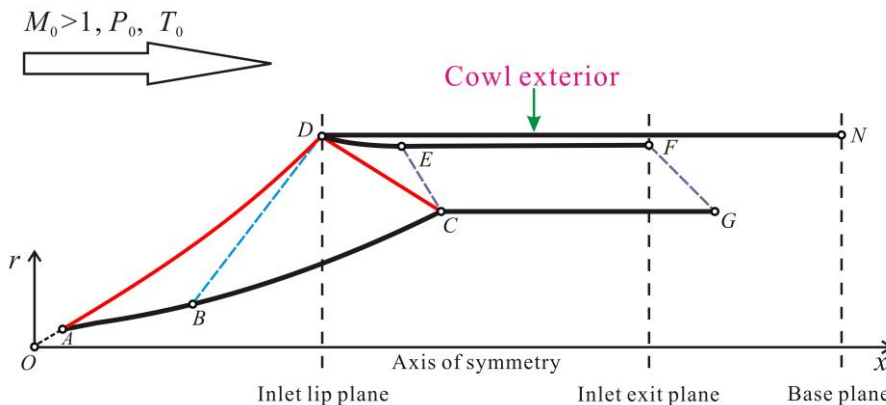
Curve 2-4-7: Leading-edge curve of forebody
Curve 2-1-7: Inlet lip curve

(b) Rear view of leading-edge curve of waverider forebody/inlet integrated vehicle and corresponding axisymmetric basic shock wave.

Figure 3 Schematic representation of the conventional waverider forebody/inlet integrated vehicle and corresponding axisymmetric basic flow model.

3.1.2 Case1_FW derived from the conventional design method of the waverider forebody/inlet integrated vehicle

Figure 3(a) illustrates one kind of forebody/inlet integrated axisymmetric basic flow model derived from an axisymmetric shock wave. This basic flow model, which is an internal and external mixed compression intake system, can be used for the design of one kind of conventional waverider forebody/inlet integrated vehicle. As can be seen in Figure 3(a), it consists of four walls and two shock waves. Unlike the model shown in Figure 1(a), the conventional model shown in Figure 3(a) does not have the afterbody basic flow region, but only has the forebody/inlet basic flow region (i.e., region *A-B-C-G-F-E-D*). The reason for this difference is that the conventional method does not take into account the waverider design of the afterbody, but only considers the waverider design of the forebody. Moreover, the forebody wall *ABC*, the centre body *CG*, the cowl interior *DEF*, and the cowl exterior *DN* make up the walls of the model. Correspondingly, the forebody shock wave *OD* and lip shock wave *DC* make up the shock wave system of this model. As this basic flow model, as shown in Figure 3(a), does not have the afterbody basic flow region, the shock wave angle of the afterbody shock wave *DR* as shown in Figure 1(a) is zero. That is to say, this conventional model is a special case of the upgraded airframe/inlet integrated basic flow model, and the vehicle generated from this basic flow model can be used as a contrast case. Moreover, the design parameters of the forebody/inlet integrated basic flow model and the leading-edge curve of the forebody for case1_FW are the same as those of case3_FW.

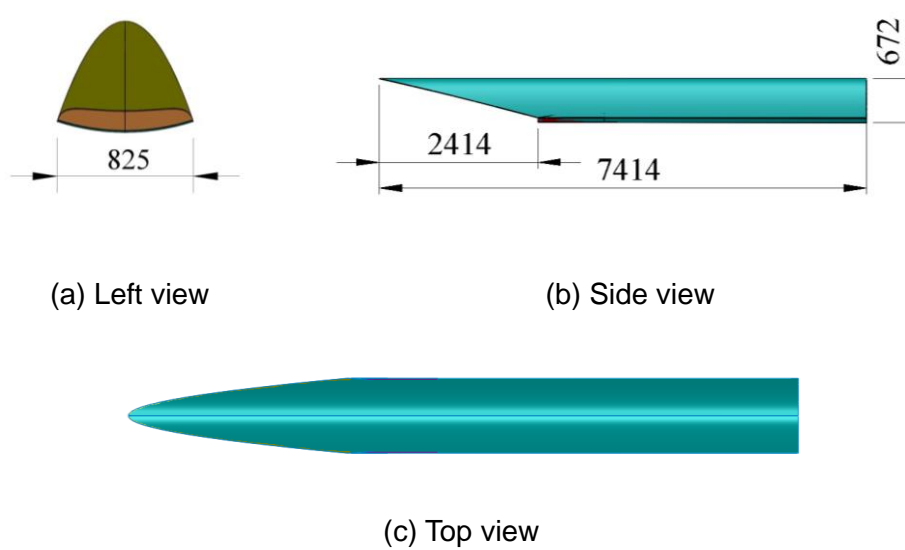(a) Left view   (b) Side view

(c) Top view

Figure 4 Geometric model of case1_FW.

The geometric model of the forebody/inlet integrated vehicle as shown in Figure 4 is generated by tracing the streamlines in the basic flow model as shown in Figure 3(a), from the leading-edge curve of the forebody (curve 2-4-7) and the inlet lip curve (curve 2-1-7) as shown in Figure 3(b) downstream, up to the inlet exit plane. This case is termed case1_FW.

3.1.3 Cases from different design parameters of the basic flow model

As the biggest highlight of the full-waverider vehicle is that both the vehicle's forebody and afterbody ride on the shock wave, it is very important to study the impact of the afterbody shock wave on the aerodynamic shape and performance of the vehicle. Furthermore, the afterbody shock wave of the vehicle depends on the design parameters of the afterbody basic flow region of the basic flow model, and these design parameters mainly include the afterbody shock wave *DR*, wall *MN* (isentropic compression or expansion wall) and the relative length of the afterbody. In this section, parameter sensitivity analysis on the aerodynamic shape and performance is carried out for the three design parameters mentioned above.
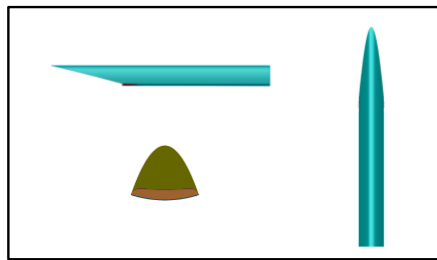
3.1.3.1 Case2_FW, case3_FW, case4_FW and case5_FW derived from different afterbody shock wave angles

Four full-waverider vehicles with different shock wave angles of the afterbody shock wave are generated, and they are termed case2_FW, case3_FW, case4_FW, and case5_FW, respectively. The comparison of geometric models between the four cases are shown in Figure 5.
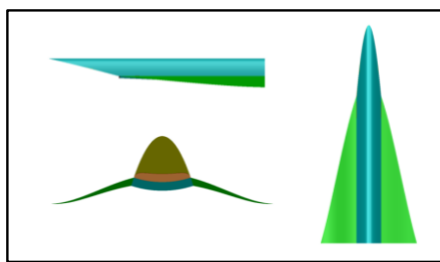
Table 1 Design values of the shock wave angle of the afterbody shock wave *DR* used for the basic flow model of case1_FW, case2_FW, case3_FW, case4_FW, and case5_FW.

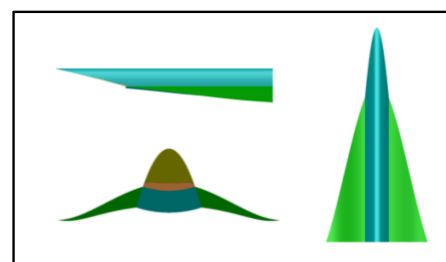|	Case1_FW	Case2_FW	Case3_FW	Case4_FW	Case5_FW
$\beta_{DR}(°)$	0.0	10.906348	13.159761	15.725442	18.557607
$\delta(°)$	0	2	5	8	11

7

The four cases' design parameters of the forebody/inlet basic flow region of the basic flow model are chosen to be the same as those of case1_FW, as are the leading-edge curves of the forebodies of the four cases, which makes the forebody/inlet of the four cases the same. A straight curve is used as the afterbody shock wave DR of the afterbody basic flow region of the basic flow model, and the design values of the shock wave angle of the afterbody shock wave DR are shown in Table 1. As can be seen in Table 1, the shock wave angles of the afterbody shock wave DR increased from 10.906348° to 18.557607°, and the flow angles just downstream of the shock wave corresponding to the four afterbody shock waves are 2°, 5°, 8° and 11°. In other words, the choice of the four shock wave angles is based on an increase of 3° in the flow angle just downstream of the shock wave. As the shock wave angles of the afterbody shock wave DR are different, the radiuses of the afterbody shock wave at the base plane are different. Therefore, in order to enhance the contrast, the dimensionless equations of the leading-edge curves of the four cases are all the same. In addition, in order to make a comparison with the conventional configuration, the four cases are also compared with case1_FW, as shown in Figure 5. As the vehicle of case1_FW does not have an afterbody waverider surface, the shock wave angle of the afterbody shock wave used in the basic flow model of case1_FW is equivalent to 0°, as can be seen in Table 1.
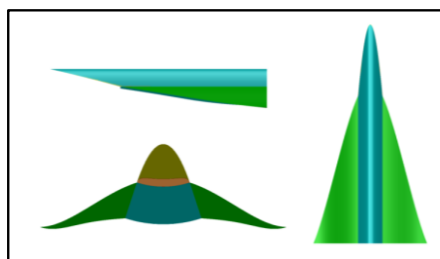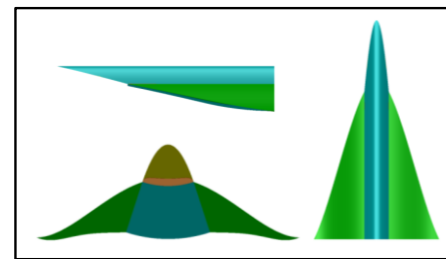

(a) Case1_FW

(b) Case2_FW

(c) Case3_FW

(d) Case4_FW

(e) Case5_FW

8

Figure 5 Comparison of geometric models between case1_FW, case2_FW, case3_FW, case4_FW, and case5_FW derived from different afterbody shock wave angles.
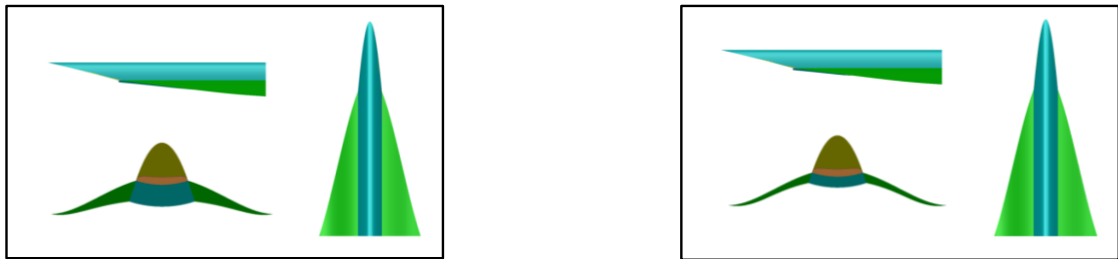
3.1.3.2 Case3_FW and case6_FW derived from different afterbody walls

As shown in Figure 1(a), the afterbody wall *MN*, which is a back segment of the cowl exterior *DN*, can determine the extent of the compression or expansion of the air after the shock wave in the afterbody basic flow region (region *D-M-N-R*). Two full-waverider vehicles with different afterbody walls *MN* are generated, and they are termed case3_FW and case6_FW, respectively. A comparison of geometric models between case3_FW and case6_FW is shown in Figure 6.

The equations of the wall *MN* for both case3_FW and case6_FW are the same. Further, when the *r* coordinates at point *N* for case3_FW and case6_FW are given in Eq. (1) and (2), respectively, the wall *MN* for both cases can be determined. Obviously, the air is less compressed by the wall *MN* of case3_FW than that of case6_FW.

$$r_N = r_M + 0.5(x_N - x_M)\tan(\delta_M) \tag{1}$$
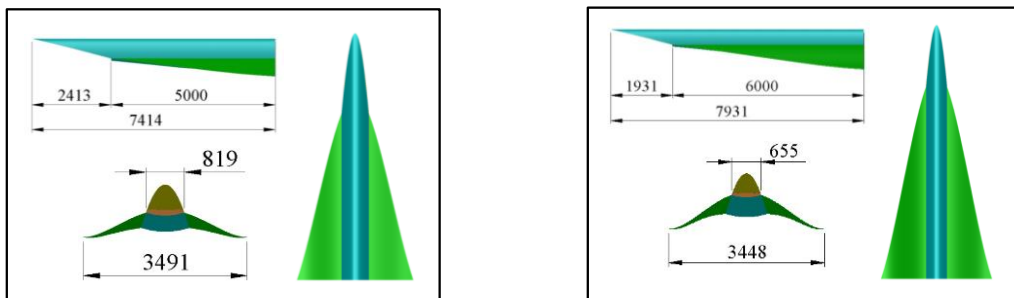
$$r_N = r_M \tag{2}$$

（a）Case3_FW   （b）Case6_FW

Figure 6 Comparison of geometric models between case3_FW and case6_FW derived from different afterbody walls *MN*.

3.1.3.3 Case3_FW and case7_FW derived from different afterbody lengths

（a）Case3_FW   （b）Case7_FW

Figure 7 Comparison of geometric models between case3_FW and case7_FW derived from different relative lengths of the afterbody.

The relative length of the afterbody accounted for the full-waverider vehicle can influence the area of the afterbody waverider surface accounted for the total lift surface of the vehicle. The effect of the area of the afterbody on the performance of the vehicle can be used to analyse the effect of the afterbody waverider on the performance of the full-waverider vehicle. Two full-waverider vehicles with different afterbody lengths are generated, and they are termed case3_FW and case7_FW. The comparison of geometric models between case3_FW and case7_FW is shown in Figure 7.

The afterbody length of the basic flow model is increased from 5 m for case3_FW to 6 m for case7_FW, and the total length of the basic flow model for both cases remain the same, i.e. 10 m.

3.2 Numerical methods

As done previously for the numerical simulation of a waverider [3][5][7] in this study, the two-equation shear-stress transport (SST) k-ω turbulence model and the 3D coupled implicit Reynolds-averaged Navier–Stokes (RANS) equations are employed to numerically simulate the viscous aerodynamic performance and flow fields of the basic flow model and the full-waverider vehicle by use of ANSYS Fluent [18]. The second-order spatially accurate upwind scheme applying the AUSM to flux vector is used, and the Green–Gauss cell-based gradient method is utilised to compute the gradients. The CFL number is set at 0.5. The enhanced wall treatment [18] is applied to the flow in the near-wall region in the selected model, and the no-slip velocity boundary condition is imposed along the walls of the model. The thermal boundary condition at the walls is considered to be adiabatic in this study.
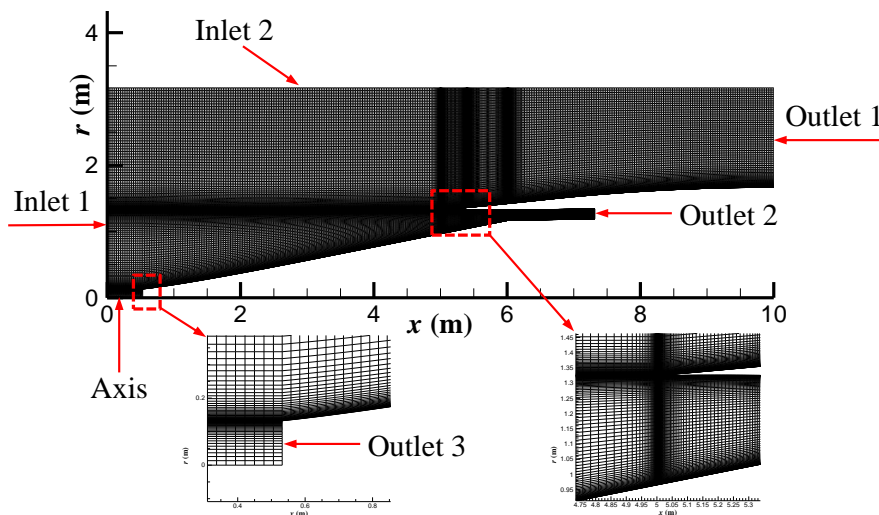

Figure 8 Schematic diagram of the structured grid and boundary conditions employed in the computational test of the airframe/inlet integrated axisymmetric basic flow model.

The iterative process and its solutions can be considered to converge if the residuals attain

minimum values, that is values less than four orders of magnitude of their original value, and when the difference between the computed inflow and outflow mass fluxes falls below 0.1%.

Euler equations are employed to numerically simulate the inviscid flow fields in the same problem formulation by use of ANSYS Fluent [18]. The Euler equations are solved using the density-based (coupled) implicit solver. The second-order spatially accurate upwind scheme applying the AUSM to the flux vector is used, and the least-squares cell-based method is utilised to compute the gradients. The CFL number is set at 0.5. As indicated previously, the air is assumed to be a thermally and calorically perfect gas. Convergence is assumed to be achieved under the same conditions as those described above.
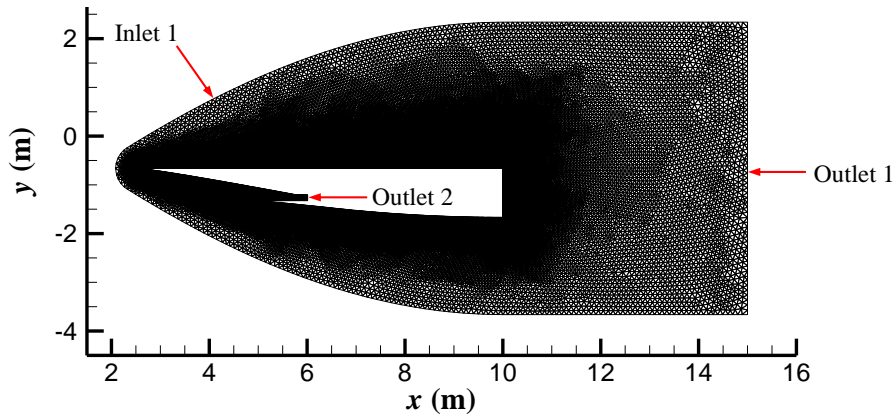

Figure 9 Schematic diagram of the unstructured grid and boundary conditions employed in the computational test of the full-waverider vehicle (plane of symmetry).

The structured grid and the inflow and outflow boundary conditions employed in the computational test of the basic flow model are shown in Figure 8. In this figure, the pressure far-field is assigned as the boundary condition of inlet 1 and inlet 2, and the pressure outlet is assigned as the boundary condition of outlet 1, outlet 2, and outlet 3. Because of the axial symmetry of the geometric configuration, only a 2D flow field is required to be solved, and the number of structured grid cells is 122,894.

The unstructured grid and the inflow and outflow boundary conditions employed in the computational test of the full-waverider vehicle are shown in Figure 9. Similarly to Figure 8, in Figure 9, the pressure far-field is assigned as the boundary condition of inlet 1 and the pressure outlet is assigned as the boundary condition of outlet 1 and outlet 2. Because of the symmetry of the geometric configuration, only half of the flow field is required to be solved, and the number of unstructured grid cells is 5,017,999.

As in our previous work [3][5][6], the specified design condition of the vehicle in this study is as follows: a cruising height of 25 km and a flight Mach number of 6.0.

11

4. Results and discussion

4.1 Validation of the design method for the full-waverider vehicle
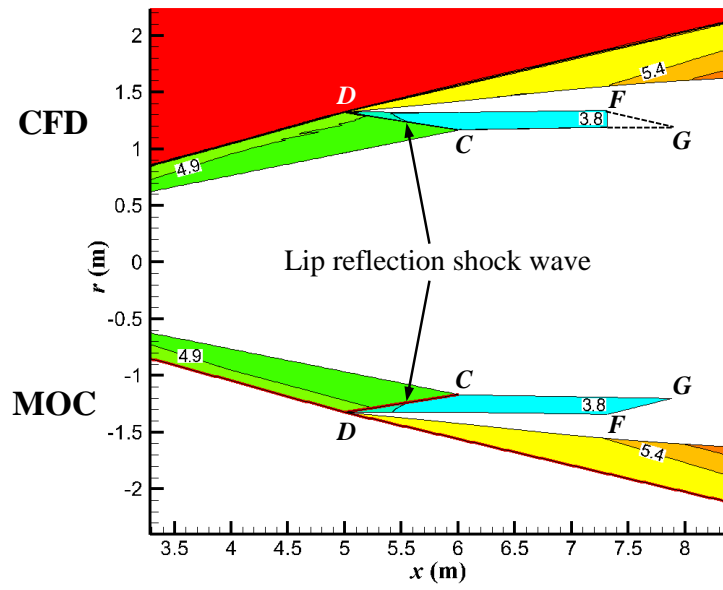
4.1.1 Validation of basic flow model

Figure 10 shows a comparison of the numerical Mach number flow field of the basic flow model for case3_FW solved by the MOC and by the Euler solver, and Figure 11 shows a comparison of the wall pressure distributions along the *x*-axis as solved by the MOC and by the Euler solver.

From Figure 10, it is clear that the numerical flow fields solved by the MOC and by the Euler solver are approximately the same. No obvious reflected shock wave forms in the shoulder region of the isolator, that is cancellation of the lip shock wave *DC* at shoulder point *C* is achieved to meet the design requirements. From Figure 11, it is obvious that there is no significant difference between the non-dimensional pressure distributions of the walls *AC*, *DE*, and *DN* solved by the MOC and by Euler solver. However, for the walls *CG* and *EF*, the pressure distributions solved by the Euler solver fluctuate near the values solved by the MOC. The possible reason for this difference is the defect of the Euler-solver-based method in mesh accuracy and shock wave resolution; specifically, the Euler-solver-based method creates a shock wave that smears over several grids, as a result of which a weak reflected shock wave may form in the shoulder region of the isolator in the numerical results obtained by the Euler-solver-based method, whereas an infinitely thin shock wave can be obtained by the MOC.
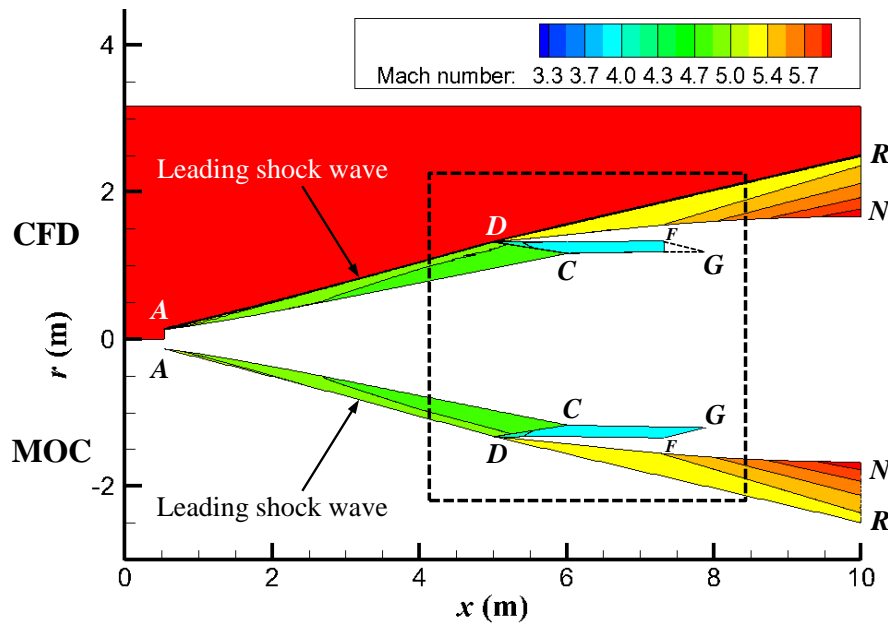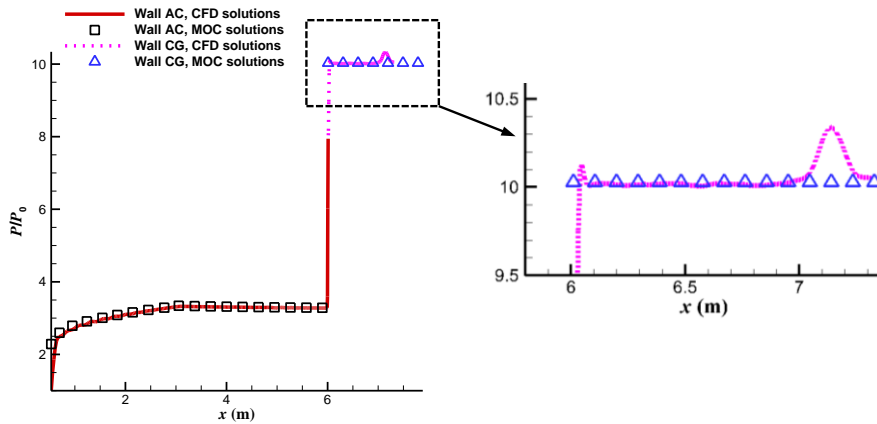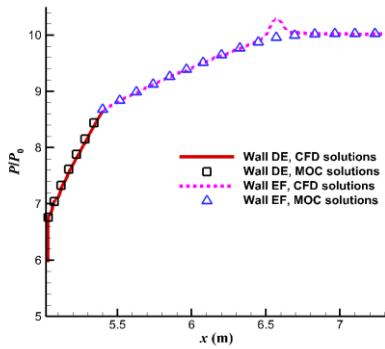

(a) Overall comparison

(b) Local comparison

Figure 10 Comparison of numerical Mach number flow field of the basic flow model solved by the MOC and by the Euler solver.
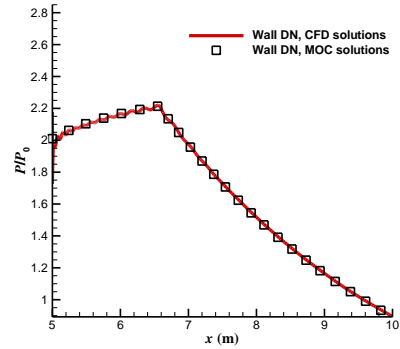
The above numerical analysis validates the design method of the basic flow model derived from an axisymmetric shock wave.

(a) Forebody wall *AC* and centre body wall *CG*

13

(b) Cowl interior DEF


(c) Cowl exterior *DN*

Figure 11 Comparison of non-dimensional wall pressure distributions of the basic flow model solved by the MOC and by the Euler solver.

4.1.2 Validation of full-waverider vehicle design

Figure 12 and Figure 13 show the inviscid flow fields on the inlet lip and base planes, and those on the axial planes of the full-waverider vehicle for case3_FW under the design condition, respectively. A comparison of the theoretical design and predicted shock wave locations is also shown in Figure 12 and Figure 13, and the theoretical design shock wave locations are represented by the dashed lines in these figures. Moreover, the axial plane is expressed by ϕ (as shown in Figure 1(c)). The axial plane at $\phi = 18°$ is the one that passes through point 2 (Figure 1(c)). The axial plane at $\phi = 0°$ is the plane of symmetry of the vehicle. The axial planes at $\phi = 0°$ and $\phi = 12°$ can be used to observe the streamwise shape of the leading-edge shock waves attached to the forebody, fuselage belly, and the lip shock wave in the inlet. Further, the axial planes at $\phi = 18°$ and $\phi = 30°$ can be used to observe the streamwise shape of the leading-edge shock wave attached to the wing.
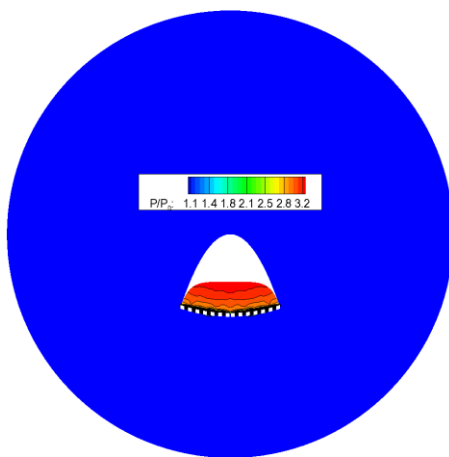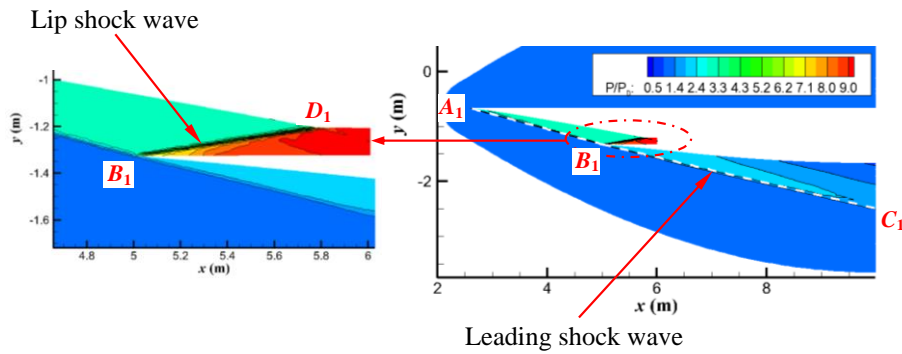

(a) Flow fields on inlet lip plane
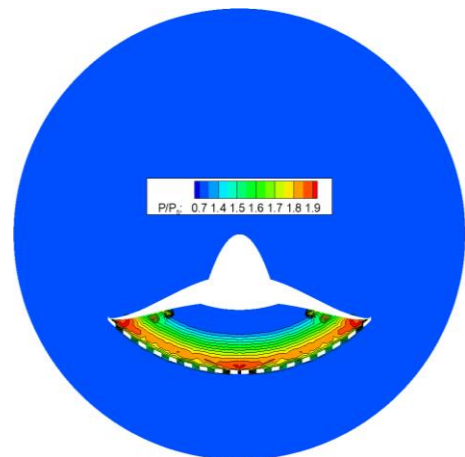
(b) Flow fields on base plane

Figure 12 Inviscid non-dimensional pressure contour lines on the lip plane and base plane of the full-waverider vehicle for case3_FW under the design conditions.

14

On both the base plane and the inlet lip plane shown in Figure 12, there is almost no leakage of high-pressure air present between the lower surface and the leading-edge shock wave to the upper surface. This indicates that not only the forebody can ride on the leading-edge shock wave (i.e. forebody waverider), but also the afterbody can ride on the leading-edge shock wave (i.e. afterbody waverider); in other words, the vehicle of case3_FW is a full-waverider. This validates the upgraded full-waverider concept proposed in this paper.

On the four chosen axial planes shown in Figure 13(a)–(d), the numerically obtained shock wave patterns containing the forebody shock wave (i.e. A_1B_1 in Figure 13(a) and A_2B_2 in Figure 13(b)), the afterbody shock wave (i.e. B_1C_1 in Figure 13(a), B_2C_2 in Figure 13(b), B_3C_3 in Figure 13(c), and B_4C_4 in Figure 13(d)), and the lip shock wave (i.e. B_1D_1 in Figure 13(a) and B_2D_2 in Figure 13(b)) are in good agreement with the basic flow model. Simultaneously, the lip shock wave is cancelled on the shoulder (i.e. point D_1 in Figure 13(a) and point D_2 in Figure 13(b)).

On the inlet lip plane, base plane, and four axial planes (Figure 12 and Figure 13), the shock wave locations predicted by the numerical method are in good agreement with the theoretical design locations. This validates the design procedure of the upgraded full-waverider vehicle in the inviscid flow field.

(a) Flow fields on symmetry plane ($\Phi = 0°$)
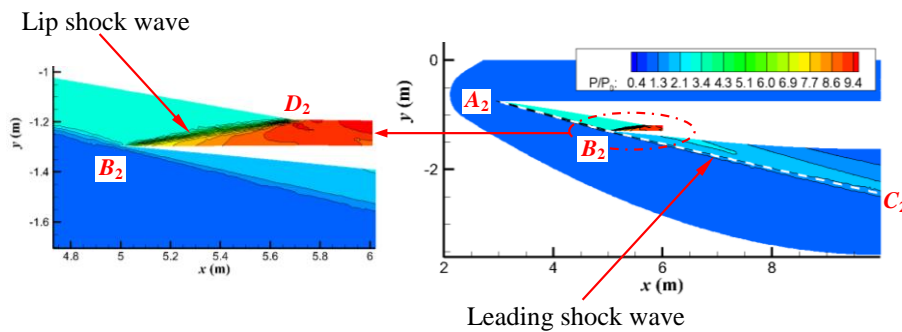
(b) Flow fields on axial plane with $\Phi = 12°$

(c) Flow fields on axial plane with $\Phi = 18°$ (d) Flow fields on axial plane with $\Phi = 30°$

Figure 13 Inviscid non-dimensional pressure contour lines on axial planes of the full-waverider vehicle for case3_FW under the design conditions.

4.2 Performance analysis and viscous effects on basic flow model

In this study, the performance parameters at the inlet exit of the basic flow model are used as the performance analysis for the basic flow model. Both the inviscid and viscous performance parameters for case3_FW are listed in Table 2. In this table, σ, $\dot{m}$, $P_{e,t}/P_{0,t}$, T_e/T_0, P_e/P_0, and M_e are all area-weighted average values on the inlet exit plane; they denote the capture mass flow coefficient, capture mass flow rate, total pressure recovery, temperature rise ratio, pressure rise ratio, and Mach number, respectively. The capture mass flow coefficient σ is evaluated as the ratio of the mass flow rate on the inlet exit plane to that on the inlet entrance plane. Moreover, both the Mach number and non-dimensional pressure contour lines under the viscous condition are shown in Figure 14.

Table 2 Comparison of inviscid and viscous performances of inlet in the basic flow model of case3_FW.

	σ	$\dot{m}$ (kg/s)	$P_{e,t}/P_{0,t}$	T_e/T_0	P_e/P_0	M_e
Inviscid	0.9975	384.7660	0.8251	2.0440	10.0593	3.8799
Viscous	0.9727	375.2207	0.5730	2.7052	12.8144	3.2849
Increment percentage	-2.5%	-2.5%	-30.6%	32.4%	27.4%	-15.3%

Several considerable differences can be seen in the shoulder region of the isolator between the viscous case (Figure 14) and the inviscid case (Figure 10); the reason for these differences is the presence of the shock wave/boundary layer interactions and viscous effects of the boundary layer. From Figure 14(a), it is observed that a small separation zone is induced by the impingement of the lip shock wave on the boundary layer of the centre body, and a corresponding reflected shock wave appears; that is, the lip shock wave does not cancel on the centre body. As a result, a well-developed shock train is established in the isolator, as shown in Figure 14(b).
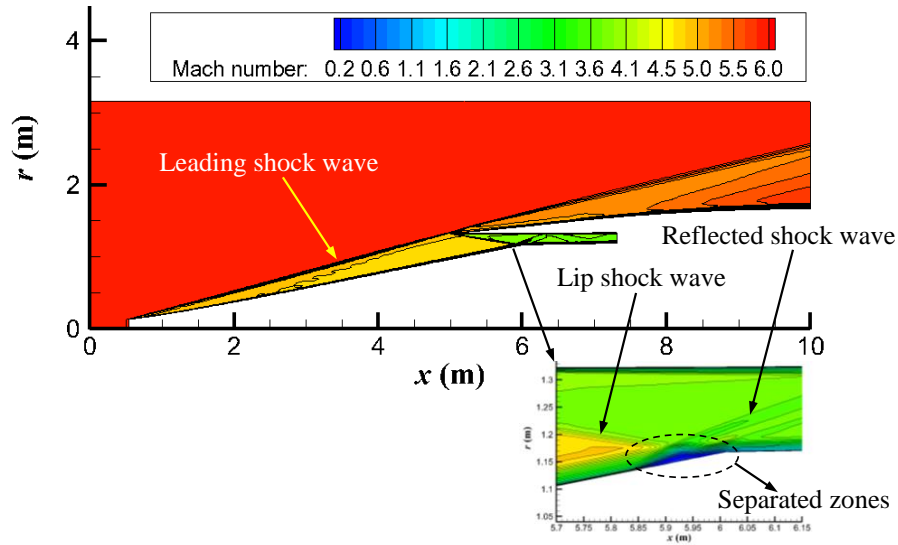
(a) Mach number contour lines
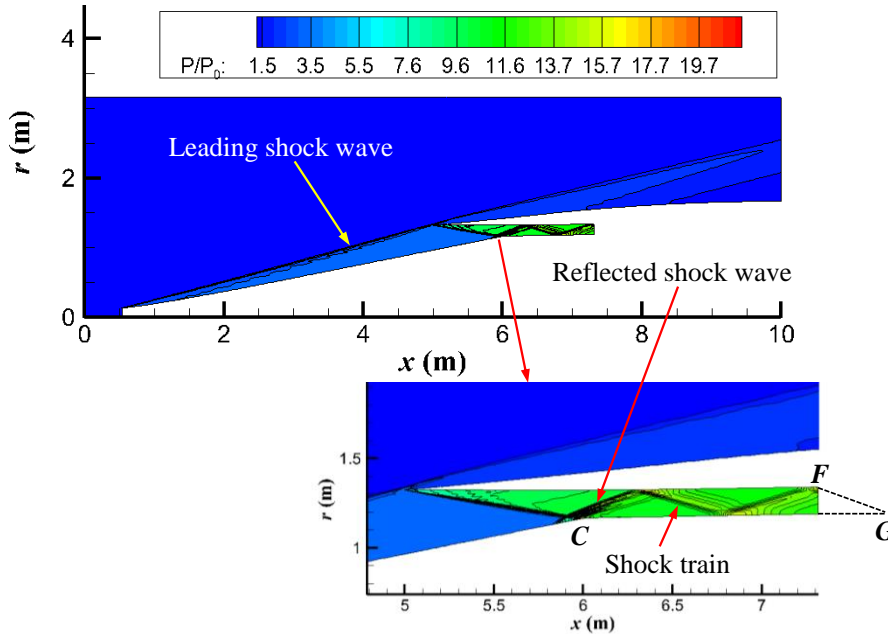
(b) Non-dimensional pressure contour lines

Figure 14 Viscous flow fields of the basic flow model for case3_FW under the design conditions.

The results in Table 2 show that the viscous effects have little influence on σ and $\dot{m}$, but a great influence on $P_{e,t}/P_{0,t}$, T_e/T_0, P_e/P_0, and M_e. The value of σ under the viscous condition is 0.9727, and it decreases by only 2.5% in comparison to the corresponding value under the inviscid condition. This indicates that even when viscous effects are considered, the shock-on-lip condition is satisfied for the basic flow model. Furthermore, when viscous effects are considered, the T_e/T_0 and P_e/P_0 ratios increase by 32.4% and 27.4%, respectively; and the values of $P_{e,t}/P_{0,t}$ and M_e decrease by 30.6% and 15.3%, respectively.

4.3 Performance analysis and viscous effects on the full-waverider vehicle

Figure 15 and Figure 16 show the viscous flow fields on the inlet lip and base planes and those on the axial planes of the full-waverider vehicle for case3_FW under the design conditions, respectively. Similar to the above invsicid analysis, a comparison of the theoretical design and predicted shock wave locations are also shown in Figure 15 and Figure 16, and the theoretical design shock wave locations are represented by the dashed lines in these figures. The performance parameters of the full-waverider vehicle are listed in Table 3. In Table 3, C_L, C_D, L/D, and C_{mz} are the lift coefficient, drag coefficient, lift-to-drag ratio, and pitching moment coefficient, respectively, and they are used as the aerodynamic force performance parameters of the entire vehicle. In addition, σ, $\dot{m}$, $P_{e,t}/P_{0,t}$, T_e/T_0, P_e/P_0, and M_e are the area-weighted average values on the inlet exit plane, and they used as the inlet performance parameters.

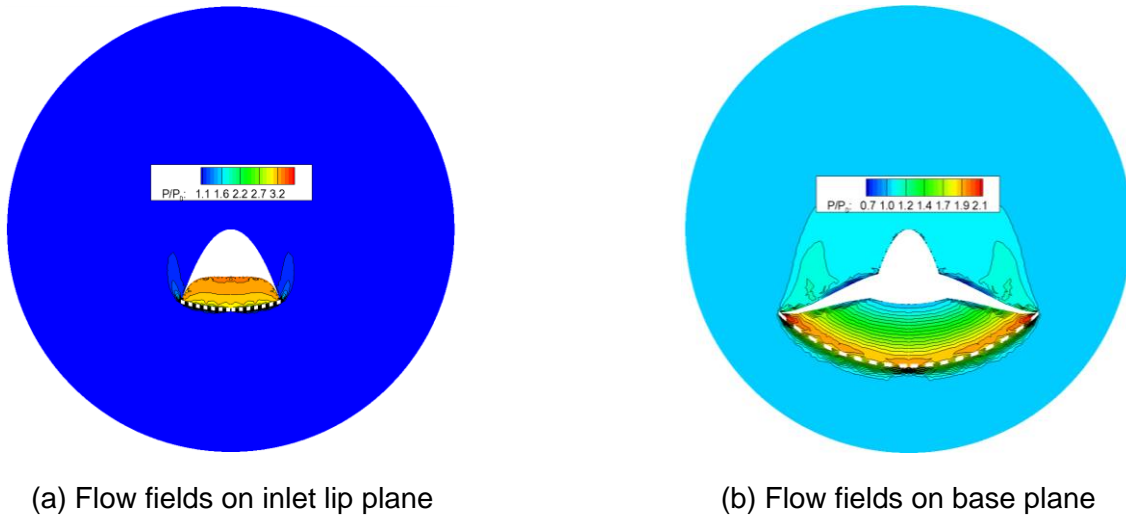(a) Flow fields on inlet lip plane   (b) Flow fields on base plane

Figure 15 Viscous non-dimensional pressure contour lines on the lip plane and base plane of the full-waverider vehicle for case3_FW under the design conditions.

From Figure 16 and Figure 13, several considerable differences can be observed in the shoulder region of the isolator between the viscous case (Figure 16 (a) and (b)) and the inviscid case (Figure 13 (a) and (b)); the reason for these differences is the presence of the shock wave/boundary layer interactions and viscous effects of the boundary layer. From Figure 16 (a) and (b), it is seen that the lip shock wave does not cancel on the shoulder (i.e. point D_1 in Figure 16 (a) and point D_2 in Figure 16 (b)), and a reflected shock wave appears. Thus, a well-developed shock train is established in the isolator.

Table 3 Comparison of inviscid and viscous performances of the full-waverider for case3_FW.

|	C_L	C_D	L/D	C_{mz}	σ	$\dot{m}$ (kg/s)	$P_{e,t}/P_{0,t}$	T_e/T_0	P_e/P_0	M_e
Inviscid	0.1805	0.0484	3.7315	-0.0158	0.9667	12.3565	0.8044	2.0261	9.3851	3.9126
Viscous	0.1967	0.0925	2.1273	-0.0184	0.9362	11.9671	0.4591	2.7794	12.7712	3.1715
Increment	9.0%	91.1%	-43.0%	16.9%	-3.2%	-3.2%	-42.9%	37.2%	36.1%	-18.9%

percentage

On the inlet lip plane, base plane, and four axial planes as shown in Figure 15 and Figure 16, owing to the presence of the boundary layer, the shock wave locations predicted by the numerical simulation deviate slightly from the locations of the theoretical design when the viscous effects is considered. Moreover, as shown in Figure 15 (a) and (b), viscous effects cause leakage of the high-pressure air from the lower surface to the upper surface, on both the inlet lip plane and the base plane.

The results in Table 3 show that the viscous effects have little impact on C_L, σ, and $\dot{m}$, but great impact on C_D, L/D, C_{mz}, $P_{e,t}/P_{0,t}$, T_e/T_0, P_e/P_0, and M_e. The value of σ under the viscous condition is 0.9362, and it decreases by only 3.2% in comparison to the corresponding value under the inviscid condition. This indicates that even when viscous effects are considered, the shock-on-lip condition is well satisfied for the full-waverider vehicle. Furthermore, when viscous effects are considered, the values of C_D, T_e/T_0, and P_e/P_0, increase by 91.1%, 37.2%, and 36.1%, respectively; and L/D, $P_{e,t}/P_{0,t}$, and M_e, decrease by 43.0%, 42.9%, and, 18.9%, respectively.
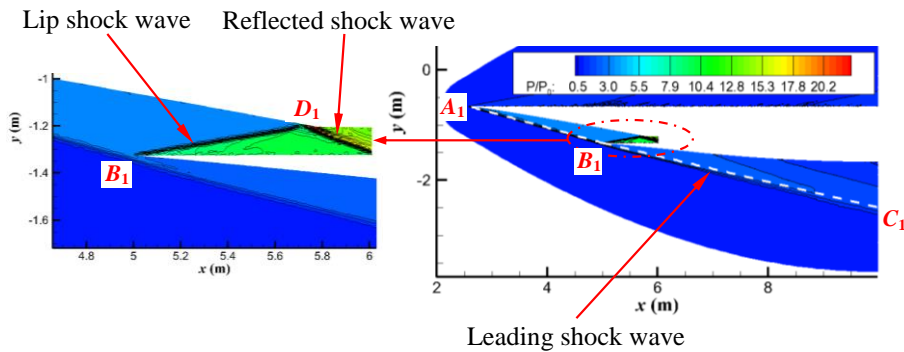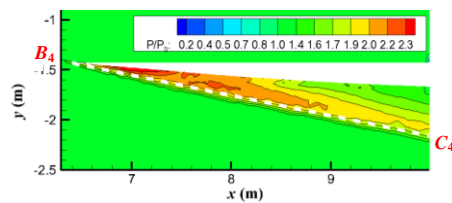

(a) Flow fields on symmetry plane ($\Phi = 0°$)
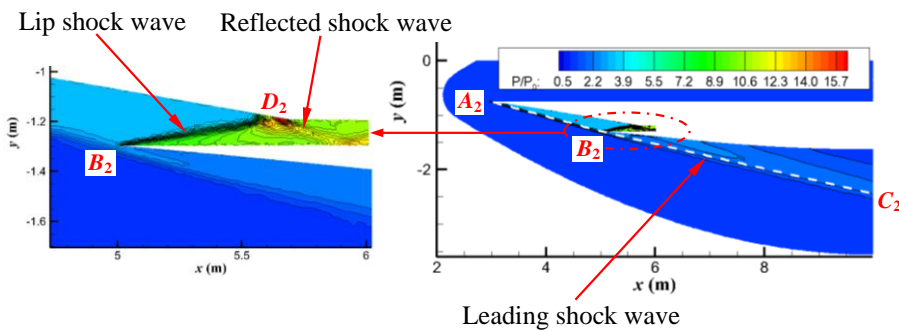
(b) Flow fields on axial plane with $\Phi = 12°$
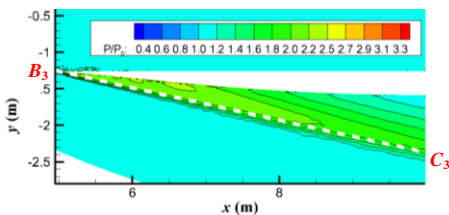
(c) Flow fields on axial plane with $\Phi = 18°$ (d) Flow fields on axial plane with $\Phi = 30°$

Figure 16 Viscous non-dimensional pressure contour lines on axial planes of the full-waverider

vehicle for case3_FW under the design conditions.

4.4 Parameter sensitivity analysis of full-waverider vehicle

4.4.1 Effect of afterbody shock wave angle on aerodynamic shape and performance

The comparisons of Mach number contour lines of basic flow models, geometric models, and aerodynamic performances for full-waverider vehicles between case1_FW, case2_FW, case3_FW, case4_FW, and case5_FW are shown in Figure 17, Figure 5 and Figure 18, respectively.

As shown in Figure 17, with an increase in the afterbody shock wave angle, the height of afterbody shock wave (i.e., radius of afterbody shock wave) at the bottom of the basic flow model and the inclination angle of the cowl exterior wall of the basic flow model increase gradually. As a result, the thickness of the vehicle as shown in Figure 5 increases with an increase in the afterbody shock wave angle, and the loading capacity of the vehicle gradually increases.

(a) Case1_FW

(b) Case2_FW

(c) Case3_FW
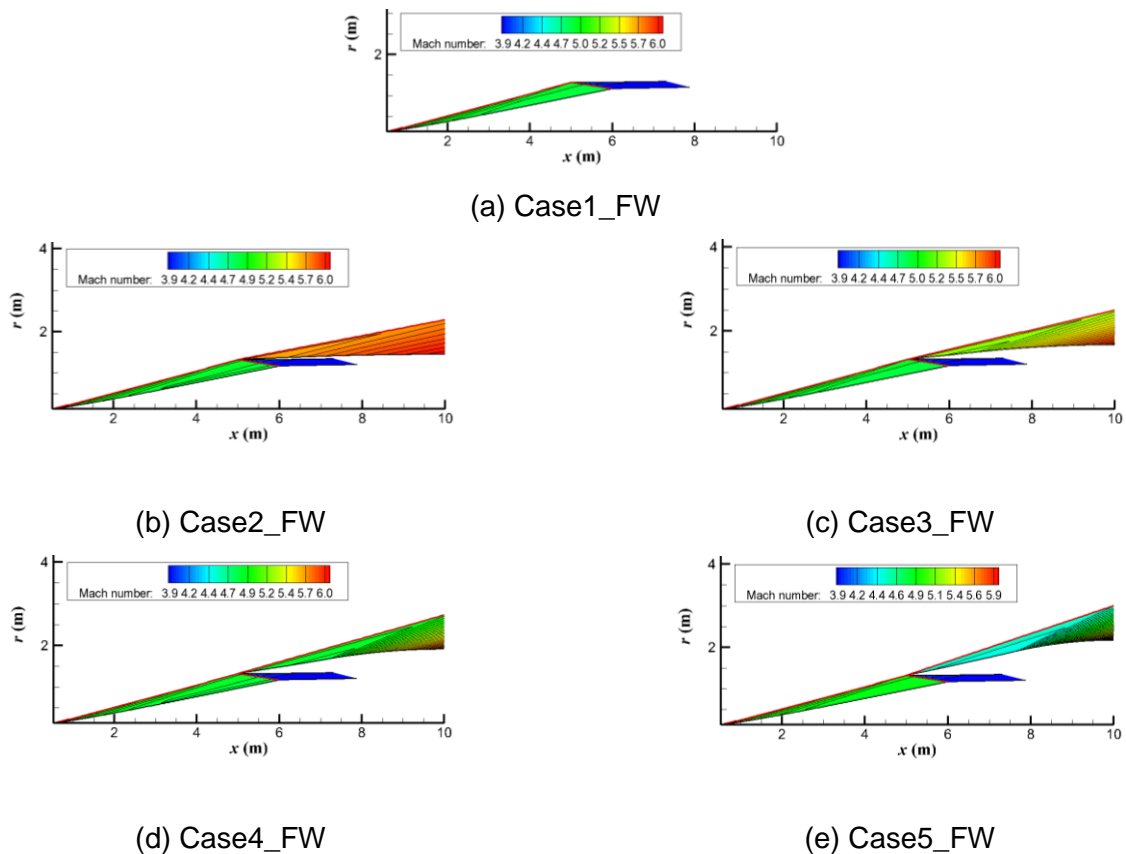

(d) Case4_FW

(e) Case5_FW

Figure 17 Comparison of Mach number contour lines of the basic flow models between case1_FW, case2_FW, case3_FW, case4_FW, and case5_FW derived from different afterbody shock wave angles.

As shown in Figure 18 (a) and (b), with an increase in the afterbody shock wave angle, the lift and drag coefficient also increase owing to the increase in the lift area and windward area of the vehicle.

As shown in Figure 18 (c), by comparing the lift-to-drag ratios of the five cases (i.e. case1_FW, case2_FW, case3_FW, case4_FW, and case5_FW), the following conclusions can be drawn:

(1) The lift-to-drag ratios of the four full-waverider vehicles (i.e. case2_FW, case3_FW, case4_FW and case5_FW) are higher than those of the conventional waverider vehicle (i.e. case1_FW) at the range of angle of attack considered, owing to the high lift-to-drag ratio characteristics of the afterbody waverider for the full-waverider vehicle.

(2) The lift-to-drag ratio of the full-waverider vehicle decreases from 3.5 for case2_FW to 2.8 for case5_FW with an increase in the afterbody shock wave angle.

(3) The angle of attack corresponding to the maximum lift-to-drag ratio decreases from 6° for case2_FW to 2° for case5_FW with an increase in the afterbody shock wave angle.

(4) The variation percentage in the lift-to-drag ratio with the angle of attack decreases with an increase in the afterbody shock wave angle. Furthermore, for case2_FW, the maximum lift-to-drag ratio is increased by 260% compared to the minimum, whereas for case5_FW, the increase percentage of lift-to-drag ratio is only 7.2%.

As shown in Figure 18 (d), the nose-down pitching moment coefficients of the four full-waverider vehicles (i.e. case2_FW, case3_FW, case4_FW, and case5_FW) are higher than those of the conventional waverider vehicle (i.e. case1_FW), owing to the air compression characteristics of the afterbody waverider for the full-waverider vehicle. Furthermore, the nose-down pitching moment coefficient of the full-waverider vehicle increases with an increase in the afterbody shock wave angle.
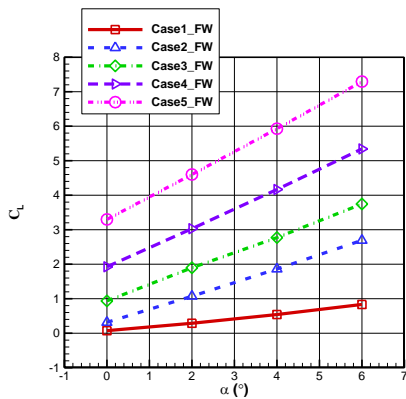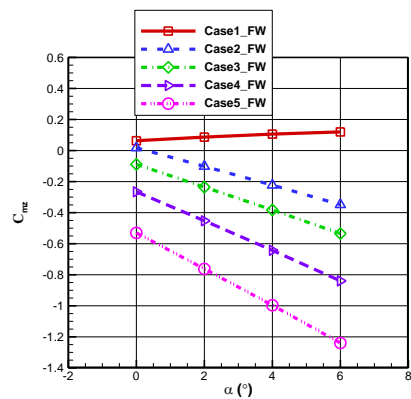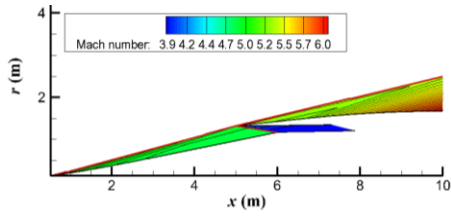

(a) Lift coefficient
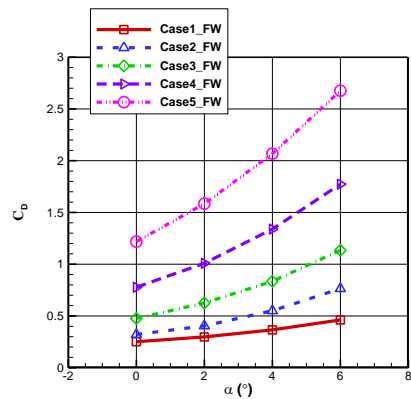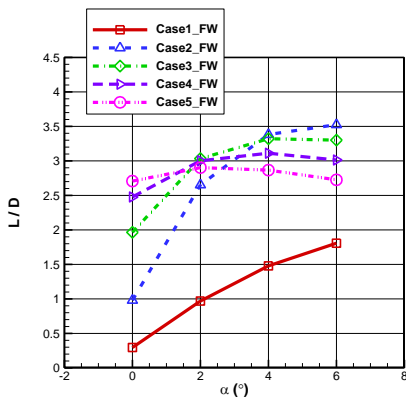
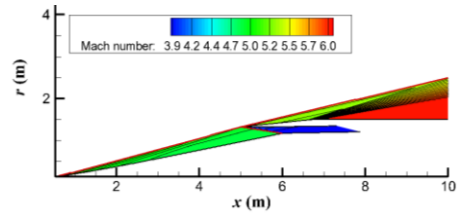(b) Drag coefficient

(c) Lift-to-drag ratio

(d) Pitching moment coefficient ($x_{cg} = 0.5$)

Figure 18 Comparison of aerodynamic performances between case1_FW, case2_FW, case3_FW, case4_FW, and case5_FW derived from different afterbody shock wave angles.
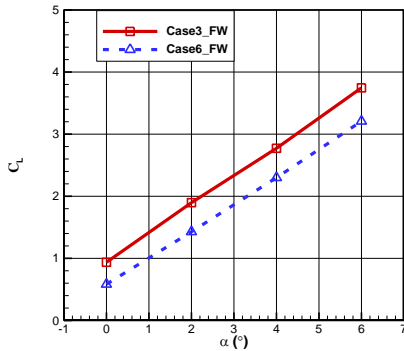

（a）Case3_FW   （b）Case6_FW
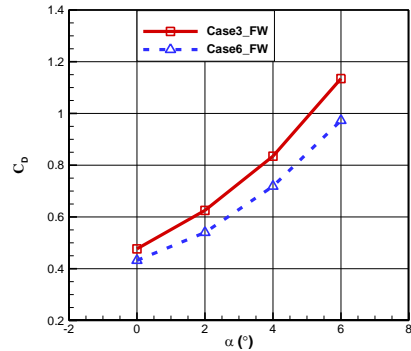
Figure 19 Comparison of Mach number contour lines of the basic flow models between case3_FW and case6_FW derived from different afterbody walls.

(a) Lift coefficient
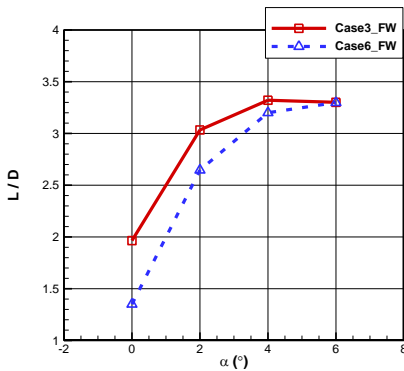
(b) Drag coefficient

(c) Lift-to-drag ratio
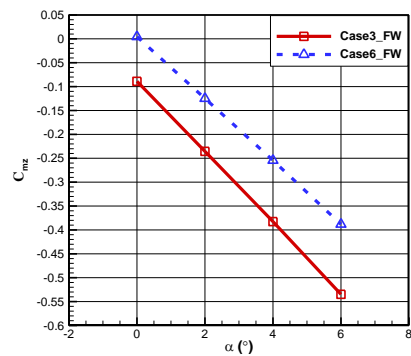
(d) Pitching moment coefficient (x_{cg} = 0.5)

Figure 20 Comparison of aerodynamic performances between case3_FW and case6_FW derived from different afterbody walls.

4.4.2 Effect of afterbody wall on aerodynamic shape and performance

The comparisons of Mach number contour lines of the basic flow models, geometric models,

and aerodynamic performances for full-waverider vehicles between case3_FW and case6_FW are shown in Figure 19, and Figure 20, respectively.

As shown in Figure 19, the expansion extent of wall *MN* against the air for case6_FW is larger than that of case3_FW. As a result, the thickness of the vehicle as shown in Figure 6 decreases with an increase in the expansion extent of wall *MN*, and the loading capacity of the vehicle also decreases accordingly.

As shown in Figure 20 (a) and (b), the lift and drag coefficient decrease with an increase in the expansion extent of wall *MN* against the air, owing to a decrease in the lift area and windward area of the vehicle.

As shown in Figure 20 (c), similar to the effect of the afterbody shock wave angle on the lift-to-drag ratio, the angle of attack corresponding to the maximum lift-to-drag ratio increases with an increase in the expansion extent of wall *MN* against the air.

As shown in Figure 20 (d), the nose-down pitching moment coefficient decreases with an increase in the expansion extent of wall *MN* against the air, owing to a decrease in the air compression by the afterbody.

4.4.3 Effect of afterbody length on aerodynamic shape and performance

The comparisons of Mach number contour lines of the basic flow models, geometric models, and aerodynamic performances for the full-waverider vehicles between case3_FW and case7_FW are shown in Figure 21, Figure 7, and Figure 22, respectively.
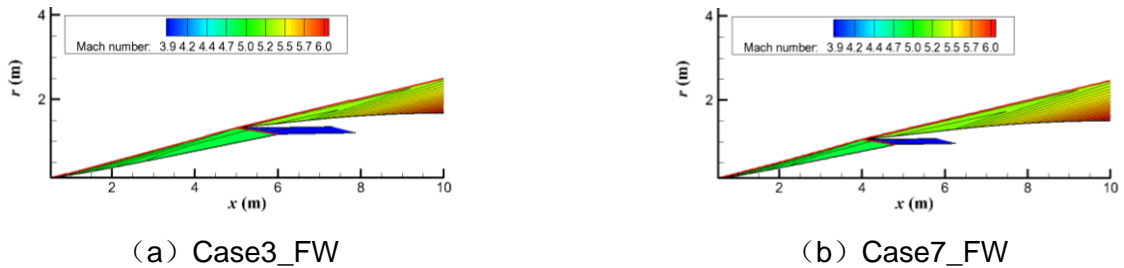

（a）Case3_FW   （b）Case7_FW

Figure 21 Comparison of Mach number contour lines of the basic flow models between case3_FW and case7_FW derived from different relative lengths of the afterbody.

As shown in Figure 21, the afterbody length of the basic flow model increases from 5 m for case3_FW to 6 m for case7_FW, and the total length of the basic flow model for both cases remain the same, i.e. 10 m. Accordingly, the length of vehicle as shown in Figure 7 is increased from 5 m for case3_FW to 6 m for case7_FW.

As shown in Figure 22 (a) and (b), the lift coefficient of case7_FW is larger than that of case3_FW, but both the drag coefficients are quite the same. The drag coefficient decreases with an increase in the expansion extent of wall *MN* against the air. This may be because the lift area of case7_FW is greater than that of case3_FW, but the windward area of the former is quite the same as that of the latter.

As shown in Figure 22 (c), the lift-to-drag ratio of the full-waverider vehicle increases with an

increase in the afterbody length. This indicates that increasing the afterbody length can better allow the advantages of afterbody waverider characteristics to be realized, and improve the lift-to-drag ratio.

As shown in Figure 22 (d), similar to the effect of the afterbody shock wave angle on the nose-down pitching moment coefficient, the nose-down pitching moment coefficient increases with an increase in the afterbody length, owing to an increase in the air compression by the afterbody.
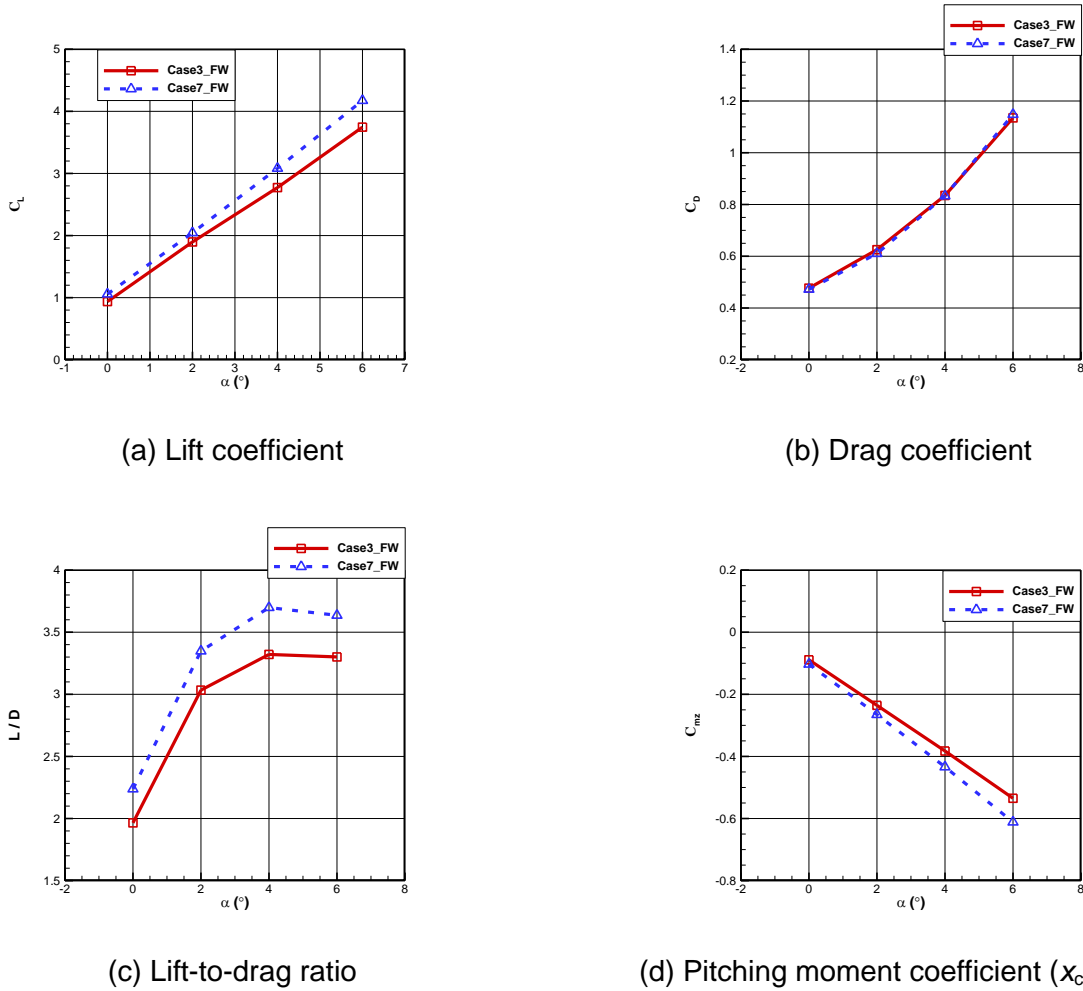

(a) Lift coefficient

(b) Drag coefficient

(c) Lift-to-drag ratio

(d) Pitching moment coefficient (x_{cg} = 0.5)

Figure 22 Comparison of aerodynamic performances between case3_FW and case7_FW derived from different relative lengths of the afterbody.

4.5 Conclusions

This paper developed an airframe/inlet integration design theory and methodology for the air-breathing hypersonic waverider vehicle. Numerical methods were employed to validate the applicability of this proposed design concept to an aerodynamic configuration. Moreover, performance analyses and viscous effects of both the basic flow model and the full-waverider vehicle were numerically predicted. Additionally, the effects of the design parameters on the aerodynamic shapes and performances were also numerically analysed. The following conclusions were drawn from these investigations.

- For the basic flow model, there is no significant difference between the wall pressure distributions obtained by the MOC and those calculated using the Euler solver, with the flow field structures being nearly identical in these two cases. Moreover, cancellation of the lip shock wave at the shoulder point is realised to meet the design requirements. This validates the design theory and methodology of the upgraded basic flow model derived from an axisymmetric basic shock wave.

- On both the base plane and the inlet lip plane of the full-waverider vehicle, there is almost no leakage of high-pressure air present between the lower surface and the leading-edge shock wave to the upper surface. This indicates that not only the forebody of the vehicle can ride on the leading-edge shock wave (i.e., forebody waverider), but also the afterbody of the vehicle can ride on the leading-edge shock wave (i.e., afterbody waverider); in other words, the vehicle is a full-waverider. This validates the design concept of the upgraded full-waverider vehicle proposed in this paper.

- On the axial planes of the full-waverider vehicle, the numerically obtained shock wave patterns containing the forebody shock wave, the afterbody shock wave, and the lip shock wave are in good agreement with the basic flow model. The shock wave locations predicted by the numerical method are in good agreement with the theoretical design locations. These results validate the design procedure of the upgraded full-waverider vehicle under the design conditions when the flow is inviscid.

- Viscous effects induce distortions at and downstream of the inlet throat, and have a great effect on the performance parameters of both the upgraded basic flow model and the upgraded full-waverider vehicle; in particular, they decrease the vehicle's lift-to-drag ratio and the inlet's total pressure recovery. Moreover, the shock-on-lip condition is satisfied well for both the upgraded basic flow model and the upgraded full-waverider vehicle under the design flight condition even when viscous effects are considered, thus enabling the inlet to efficiently capture the precompression air flow.

- Parameter sensitivity analysis shows that the waverider afterbody is a major factor in the lift-to-drag ratio of the full-waverider vehicle, and the lift-to-drag ratio of the full-waverider vehicle is higher than that of the conventional waverider vehicle, owing to the high lift-to-drag ratio characteristics of the waverider afterbody.

- Decreasing the afterbody shock wave angle of the basic flow model, increasing the expansion extent of wall *MN* of the basic flow model, or increasing the afterbody length of the basic flow model can increase the lift-to-drag ratio of the full-waverider vehicle.

- The results obtained from this study demonstrate that the full-waverider approach is effective in designing the airframe/inlet integrated waverider vehicle.

5. Contact Author Email Address

Email address of corresponding author Shanguang Guo: shanguang_guo@163.com.

6. Copyright Statement

The authors confirm that they, and/or their company or organization, hold copyright on all of the original material included in this paper. The authors also confirm that they have obtained permission, from the copyright holder of any third party material included in this paper, to publish it as part of their paper. The authors confirm that they give permission, or have obtained permission from the copyright holder of this paper, for the publication and distribution of this paper as part of the ICAS proceedings or as individual off-prints from the proceedings.

7. Acknowledgements

References

[1] O'Neill M K. Optimized scramjet engine integration on a waverider airframe. College Park, MD: University of Maryland College Park (Ph.D.), 1992.

[2] O'Neill M K and M Lewis J. Optimized scramjet integration on a waverider. Journal of Aircraft, Vol. 29, No. 6, pp. 1114–1121, 1992.

[3] Ding F, Liu J, Shen C –b and Huang W. Novel inlet-airframe integration methodology for hypersonic waverider vehicles. Acta Astronauta, Vol. 111, pp. 178–197, 2015.

[4] Nonweiler T R F. Aerodynamic problems of manned space vehicles. J. Royal Aeronaut. Soc, Vol. 63, pp. 521–528, 1959.

[5] Ding F, Liu J, Huang W, Peng C and Shen C –b. An Airframe/inlet Integrated Full-waverider Vehicle Design Using as Upgraded Aerodynamic Method. The Aeronautical Journal, Vol. 123, No. 1266, pp. 1135–1169, 2019.

[6] Ding F, Liu J, Shen C -b, Liu Z, Chen S –h and Huang W. Experimental Investigation of a Novel Airframe–Inlet Integrated Full-Waverider Vehicle. AIAA Journal, Vol. 57, No. 7, pp. 2964–2976.

[7] Ding F, Shen C -b, Liu J and Huang W. Influence of surface pressure distribution of basic flow field on shape and performance of waverider. Acta Astronauta, Vol. 108, pp. 62–78, 2015.

[8] Ding F, Liu J, Shen C -b and Huang W. Novel approach for design of a waverider vehicle generated from axisymmetric supersonic flows past a pointed von Karman ogive. Aerospace Science and Technology. Vol. 42, pp. 297–308, 2015.

[9] Lobbia M A and Suzuki K. Experimental investigation of a Mach 3.5 waverider designed using computaional fluid dynamics. AIAA Journal, Vol. 53, No. 6, pp. 1590–1601, 2015.

[10] Cui K, Li G -L, Xiao Y and Xu Y -Z. High-pressure capturing wing configurations. AIAA Journal, Vol. 55, No. 6, pp. 1909–1919, 2017.

[11] Ding,F Liu J, Shen C -b, Liu Z, Chen S –h and Fu X. An overview of research on waverider design methodology. Acta Astronauta, Vol. 140, pp. 190-205, 2017.

[12] Ding F, Liu J, Shen C -b, Huang W, Liu Z and Chen S –h. An overview of waverider design concept in airframe/inlet integration methodology for air-breathing hypersonic vehicles. Acta Astronauta, Vol. 152, pp. 639–656, 2018.

[13] Wang X D, Wang J F and Lyu Z J. A new integration method based on the coupling of mutistage osculating cones waverider and Busemann inlet for hypersonic airbreathing vehicles. Acta Astronauta, Vol. 126, pp. 424–438, 2016.

[14] He X Z., Le J L, Zhou Z and Wei F. Progress in waverider inlet integration study. AIAA Paper 2015-3685, 2015.

[15] Rodi P E. Preliminary ramjet/scramjet integration with vehicles using osculating flowfields waverider forebodies. AIAA Paper 2012-3223, 2012.

[16] You Y C, Zhu C X and Guo J L. Dual waverider concept for the integration of hypersonic inward-turning inlet and airframe forebody. AIAA Paper 2009-7421, 2009.

[17] Li Y Q, An P, Pan C J, Chen R Q and You Y C. Integration methodology for waverider-derived hypersonic inlet and vehicle forebody. AIAA Paper 2014-3229, 2014.

[18] Fluent Inc., ANSYS, Inc., ANSYS FLUENT 13.0 Theory Guide, 2010.